

## Atmospheric neutrino oscillation analysis with subleading effects in Super-Kamiokande I, II, and III

R. Wendell,<sup>9</sup> C. Ishihara,<sup>2</sup> K. Abe,<sup>1</sup> Y. Hayato,<sup>1,3</sup> T. Iida,<sup>1</sup> M. Ikeda,<sup>1</sup> K. Iyogi,<sup>1</sup> J. Kameda,<sup>1</sup> K. Kobayashi,<sup>1</sup> Y. Koshio,<sup>1</sup> Y. Kozuma,<sup>1</sup> M. Miura,<sup>1</sup> S. Moriyama,<sup>1,3</sup> M. Nakahata,<sup>1,3</sup> S. Nakayama,<sup>1</sup> Y. Obayashi,<sup>1</sup> H. Ogawa,<sup>1</sup> H. Sekiya,<sup>1</sup> M. Shiozawa,<sup>1,3</sup> Y. Suzuki,<sup>1,3</sup> A. Takeda,<sup>1</sup> Y. Takenaga,<sup>1</sup> Y. Takeuchi,<sup>1,3</sup> K. Ueno,<sup>1</sup> K. Ueshima,<sup>1</sup> H. Watanabe,<sup>1</sup> S. Yamada,<sup>1</sup> T. Yokozawa,<sup>1</sup> S. Hazama,<sup>2</sup> H. Kaji,<sup>2</sup> T. Kajita,<sup>2,3</sup> K. Kaneyuki,<sup>2,3</sup> T. McLachlan,<sup>2</sup> K. Okumura,<sup>2</sup> Y. Shimizu,<sup>2</sup> N. Tanimoto,<sup>2</sup> M. R. Vagins,<sup>3,6</sup> F. Dufour,<sup>4</sup> E. Kearns,<sup>4,3</sup> M. Litos,<sup>4</sup> J. L. Raaf,<sup>4</sup> J. L. Stone,<sup>4,3</sup> L. R. Sulak,<sup>4</sup> W. Wang,<sup>4,\*</sup> M. Goldhaber,<sup>5</sup> K. Bays,<sup>6</sup> D. Casper,<sup>6</sup> J. P. Cravens,<sup>6</sup> W. R. Kropp,<sup>6</sup> S. Mine,<sup>6</sup> C. Regis,<sup>6</sup> M. B. Smy,<sup>6,3</sup> H. W. Sobel,<sup>6,3</sup> K. S. Ganezer,<sup>7</sup> J. Hill,<sup>7</sup> W. E. Keig,<sup>7</sup> J. S. Jang,<sup>8</sup> J. Y. Kim,<sup>8</sup> I. T. Lim,<sup>8</sup> J. Albert,<sup>9</sup> M. Fechner,<sup>9,†</sup> K. Scholberg,<sup>9,3</sup> C. W. Walter,<sup>9,3</sup> S. Tasaka,<sup>10</sup> J. G. Learned,<sup>11</sup> S. Matsuno,<sup>11</sup> Y. Watanabe,<sup>12</sup> T. Hasegawa,<sup>13</sup> T. Ishida,<sup>13</sup> T. Ishii,<sup>13</sup> T. Kobayashi,<sup>13</sup> T. Nakadaira,<sup>13</sup> K. Nakamura,<sup>13,3</sup> K. Nishikawa,<sup>13</sup> H. Nishino,<sup>13</sup> Y. Oyama,<sup>13</sup> K. Sakashita,<sup>13</sup> T. Sekiguchi,<sup>13</sup> T. Tsukamoto,<sup>13</sup> A. T. Suzuki,<sup>14</sup> A. Minamino,<sup>15</sup> T. Nakaya,<sup>15,3</sup> Y. Fukuda,<sup>16</sup> Y. Itow,<sup>17</sup> G. Mitsuka,<sup>17</sup> T. Tanaka,<sup>17</sup> C. K. Jung,<sup>18</sup> G. Lopez,<sup>18</sup> C. McGrew,<sup>18</sup> C. Yanagisawa,<sup>18</sup> N. Tamura,<sup>19</sup> H. Ishino,<sup>20</sup> A. Kibayashi,<sup>20</sup> S. Mino,<sup>20</sup> T. Mori,<sup>20</sup> M. Sakuda,<sup>20</sup> H. Toyota,<sup>20</sup> Y. Kuno,<sup>21</sup> M. Yoshida,<sup>21</sup> S. B. Kim,<sup>22</sup> B. S. Yang,<sup>22</sup> T. Ishizuka,<sup>23</sup> H. Okazawa,<sup>24</sup> Y. Choi,<sup>25</sup> K. Nishijima,<sup>26</sup> Y. Yokosawa,<sup>26</sup> M. Koshiba,<sup>27</sup> M. Yokoyama,<sup>27</sup> Y. Totsuka,<sup>27,‡</sup> S. Chen,<sup>28</sup> Y. Heng,<sup>28</sup> Z. Yang,<sup>28</sup> H. Zhang,<sup>28</sup> D. Kielczewska,<sup>29</sup> P. Mijakowski,<sup>29</sup> K. Connolly,<sup>30</sup> M. Dziomba,<sup>30</sup> E. Thrane,<sup>30,§</sup> and R. J. Wilkes<sup>30</sup>

(The Super-Kamiokande Collaboration)

<sup>1</sup>*Kamioka Observatory, Institute for Cosmic Ray Research, University of Tokyo, Kamioka, Gifu 506-1205, Japan*

<sup>2</sup>*Research Center for Cosmic Neutrinos, Institute for Cosmic Ray Research, University of Tokyo, Kashiwa, Chiba 277-8582, Japan*

<sup>3</sup>*Institute for the Physics and Mathematics of the Universe, University of Tokyo, Kashiwa, Chiba 277-8582, Japan*

<sup>4</sup>*Department of Physics, Boston University, Boston, Massachusetts 02215, USA*

<sup>5</sup>*Physics Department, Brookhaven National Laboratory, Upton, New York 11973, USA*

<sup>6</sup>*Department of Physics and Astronomy, University of California, Irvine, Irvine, California 92697-4575, USA*

<sup>7</sup>*Department of Physics, California State University, Dominguez Hills, Carson, California 90747, USA*

<sup>8</sup>*Department of Physics, Chonnam National University, Kwangju 500-757, Korea*

<sup>9</sup>*Department of Physics, Duke University, Durham North Carolina 27708, USA*

<sup>10</sup>*Department of Physics, Gifu University, Gifu, Gifu 501-1193, Japan*

<sup>11</sup>*Department of Physics and Astronomy, University of Hawaii, Honolulu, Hawaii 96822, USA*

<sup>12</sup>*Physics Division, Department of Engineering, Kanagawa University, Kanagawa, Yokohama 221-8686, Japan*

<sup>13</sup>*High Energy Accelerator Research Organization (KEK), Tsukuba, Ibaraki 305-0801, Japan*

<sup>14</sup>*Department of Physics, Kobe University, Kobe, Hyogo 657-8501, Japan*

<sup>15</sup>*Department of Physics, Kyoto University, Kyoto, Kyoto 606-8502, Japan*

<sup>16</sup>*Department of Physics, Miyagi University of Education, Sendai, Miyagi 980-0845, Japan*

<sup>17</sup>*Solar Terrestrial Environment Laboratory, Nagoya University, Nagoya, Aichi 464-8602, Japan*

<sup>18</sup>*Department of Physics and Astronomy, State University of New York, Stony Brook, New York 11794-3800, USA*

<sup>19</sup>*Department of Physics, Niigata University, Niigata, Niigata 950-2181, Japan*

<sup>20</sup>*Department of Physics, Okayama University, Okayama, Okayama 700-8530, Japan*

<sup>21</sup>*Department of Physics, Osaka University, Toyonaka, Osaka 560-0043, Japan*

<sup>22</sup>*Department of Physics, Seoul National University, Seoul 151-742, Korea*

<sup>23</sup>*Department of Systems Engineering, Shizuoka University, Hamamatsu, Shizuoka 432-8561, Japan*

<sup>24</sup>*Department of Informatics in Social Welfare, Shizuoka University of Welfare, Yaizu, Shizuoka, 425-8611, Japan*

<sup>25</sup>*Department of Physics, Sungkyunkwan University, Suwon 440-746, Korea*

<sup>26</sup>*Department of Physics, Tokai University, Hiratsuka, Kanagawa 259-1292, Japan*

<sup>27</sup>*The University of Tokyo, Bunkyo, Tokyo 113-0033, Japan*

<sup>28</sup>*Department of Engineering Physics, Tsinghua University, Beijing, 100084, China*

<sup>29</sup>*Institute of Experimental Physics, Warsaw University, 00-681 Warsaw, Poland*

<sup>30</sup>*Department of Physics, University of Washington, Seattle, Washington 98195-1560, USA*

\*Present address: Department of Physics, University of Wisconsin-Madison, 1150 University Avenue, Madison, WI 53706, USA

†Present address: CEA, Irfu, SPP, Centre de Saclay, F-91191, Gif-sur-Yvette, France

‡Deceased

§Present address: School of Physics and Astronomy, University of Minnesota, 116 Church Street S.E., Minneapolis, MN 55455, USA

(Received 18 February 2010; published 20 May 2010)

We present a search for nonzero  $\theta_{13}$  and deviations of  $\sin^2\theta_{23}$  from 0.5 in the oscillations of atmospheric neutrino data from Super-Kamiokande I, II, and III. No distortions of the neutrino flux consistent with nonzero  $\theta_{13}$  are found and both neutrino mass hierarchy hypotheses are in agreement with the data. The data are best fit at  $\Delta m^2 = 2.1 \times 10^{-3} \text{ eV}^2$ ,  $\sin^2\theta_{13} = 0.0$ , and  $\sin^2\theta_{23} = 0.5$ . In the normal (inverted) hierarchy  $\theta_{13}$  and  $\Delta m^2$  are constrained at the one-dimensional 90% C.L. to  $\sin^2\theta_{13} < 0.04(0.09)$  and  $1.9(1.7) \times 10^{-3} < \Delta m^2 < 2.6(2.7) \times 10^{-3} \text{ eV}^2$ . The atmospheric mixing angle is within  $0.407 \leq \sin^2\theta_{23} \leq 0.583$  at 90% C.L.

DOI: 10.1103/PhysRevD.81.092004

PACS numbers: 14.60.Pq, 96.50.S-

## I. INTRODUCTION

Despite experimental measurements of solar [1–8], reactor [9], atmospheric [10,11], and accelerator [12,13] neutrinos constraining their flavor oscillations, the nature of the neutrino mass hierarchy and whether or not  $\theta_{13}$  is zero remain open questions. The latter is the last unknown mixing angle and is currently the subject of a research program including beam and reactor-based experiments [14–19]. At present, experiments have placed upper limits on the value of  $\theta_{13}$  [10,20–22] with the most stringent limit set by the Chooz [23] experiment. However, a nonzero value may manifest itself and be observable in the event rate of multi-GeV electron neutrinos passing through the Earth and, to a lesser extent, in similarly energetic upward-going muon samples. Though atmospheric neutrino data are well fit to pure  $\nu_\mu \leftrightarrow \nu_\tau$  oscillations with “maximal atmospheric mixing” [11] ( $\theta_{23} = \pi/4$ ),  $\nu_\mu \leftrightarrow \nu_e$  transitions driven by solar oscillation parameters appear at sub-GeV energies when the atmospheric mixing deviates from this value. The questions of whether or not  $\theta_{23}$  is exactly  $\pi/4$ , the nature of  $\theta_{13}$ , and the sign of the neutrino mass hierarchy all contribute to an eight-fold degeneracy [24] of oscillation parameter solutions when considering  $CP$ -violation in neutrinos. For future experimental searches of  $CP$ -violation, answers to these questions are essential.

In this paper two analyses are presented, searching for evidence of subleading (second order) oscillation effects which address these questions and appear as changes in the  $\nu_e$  and  $\nu_\mu$  fluxes of the atmospheric neutrino samples at Super-Kamiokande (Super-K, SK). The first is an improved extension of a three-flavor oscillation analysis using the first phase of the experiment (SK-I) [10]. An updated analysis using the first, second (SK-II), and third (SK-III) phases is presented here. The data are then used in the second analysis to test whether  $\theta_{23}$  deviates from  $\pi/4$ .

The paper is organized as follows. In Sec. II we describe the oscillation framework used in the analyses. Section III discusses the data sample including additional sample selections designed to improve the sensitivity of each analysis. The methods and results of both are then presented in Sec. IV and concluding remarks are found in Sec. V.

## II. SUBDOMINANT EFFECTS IN ATMOSPHERIC NEUTRINO OSCILLATIONS

Neutrino oscillations in three flavors are described by six parameters: two mass squared differences,  $\Delta m_{12}^2$ ,  $\Delta m_{13}^2$ , where  $\Delta m_{ij}^2 = m_j^2 - m_i^2$ , a  $CP$  violating parameter  $\delta_{cp}$ , and three mixing angles  $\theta_{ij}$  ( $i < j$ ). Each mixing angle parametrizes a rotation,  $U_{ij}$ , between mass states inside of the three-dimensional oscillation space. The correspondence between neutrino mass eigenstates and their flavor eigenstates is then

$$|\nu_\alpha\rangle = \sum_i^3 U_{\alpha,i}^* |\nu_i\rangle, \quad (1)$$

where  $U$  is the  $3 \times 3$  Pontecorvo-Maki-Nakagawa-Sakata (PMNS) matrix [25,26] defined by  $U_{23}U_{13}U_{12}$ ,

$$U = \begin{pmatrix} 1 & 0 & 0 \\ 0 & c_{23} & s_{23} \\ 0 & -s_{23} & c_{23} \end{pmatrix} \begin{pmatrix} c_{13} & 0 & s_{13}e^{-i\delta_{cp}} \\ 0 & 1 & 0 \\ -s_{13}e^{i\delta_{cp}} & 0 & c_{13} \end{pmatrix} \times \begin{pmatrix} c_{12} & s_{12} & 0 \\ -s_{12} & c_{12} & 0 \\ 0 & 0 & 1 \end{pmatrix}. \quad (2)$$

Nonzero mixing angles and nondegenerate mass eigenvalues give rise to standard neutrino oscillations. Observations of solar and reactor neutrinos are well-described by oscillations governed by the “1–2” (solar) parameters while those of atmospheric and accelerator neutrinos are described by the “2–3” (atmospheric) parameters. These measurements have established two oscillation frequencies which differ by a factor of  $\sim 30$ . The third set of parameters has been probed by Chooz, a reactor neutrino disappearance experiment sensitive to oscillations at the atmospheric  $\Delta m^2$ , which placed a limit on mixing in this channel at  $\sin^2\theta_{13} < 0.04$  for  $\Delta m^2 \sim 2.0 \times 10^{-3} \text{ eV}^2$  at 90% confidence [23].

For the purposes of studying subdominant oscillations in atmospheric neutrinos, it is useful to consider oscillation probabilities in two domains: (i)  $\theta_{13} \sim 0$  such that  $U_{13} \sim \mathbf{I}$ , and (ii)  $\theta_{13} > 0$ , but oscillations driven by the solar parameters are negligible. The observable effects each

domain has on the atmospheric neutrino sample can similarly be divided into two energy regimes motivating two separate analyses with distinct foci: each analysis has been tailored to its regime of interest.

In the case of  $\theta_{13} \sim 0$ , the neutrino oscillation probabilities in constant density matter may be written [27]

$$P(\nu_e \leftrightarrow \nu_\mu) = \cos^2 \theta_{23} P_{ex} \quad (3)$$

$$P(\nu_\mu \leftrightarrow \nu_\mu) = 1 - \cos^4 \theta_{23} P_{ex} - \sin^2 2\theta_{23} (1 - \sqrt{1 - P_{ex}} \cos \phi) \quad (4)$$

$$\phi \sim (\Delta m_{31}^2 + s_{12}^2 \Delta m_{21}^2) \frac{L}{2E_\nu},$$

where  $P_{ex}$  is the two neutrino transition probability ( $\nu_e \rightarrow \nu_x$ ) driven by  $\Delta m_{12}^2$  and  $\theta_{12}$ ,  $L$  is the neutrino path length, and  $E$  is its energy. Using these equations the modified atmospheric  $\nu$  fluxes at Super-K become

$$\Phi_e = \Phi_e^0 [1 + P_{ex}(r \cos^2 \theta_{23} - 1)]$$

$$\Phi_\mu = \Phi_\mu^0 \left[ 1 - \frac{\cos^2 \theta_{23}}{r} (r \cos^2 \theta_{23} - 1) P_{ex} \right] - \frac{\Phi_\mu^0}{2} \sin^2 2\theta_{23} (1 - \sqrt{1 - P_{ex}} \cos \phi), \quad (5)$$

where  $\Phi_\mu^0$  and  $\Phi_e^0$  are the neutrino fluxes in the absence of oscillations and  $r$  is their ratio.

The left panel in Fig. 1 shows the transition probability,  $P_{ex}$ , as a function of energy and zenith angle,  $\Theta_\nu$ , for neutrinos traversing the Earth (see below) assuming  $\Delta m_{12}^2 = 7.7 \times 10^{-5} \text{ eV}^2$  and  $\sin^2 \theta_{12} = 0.30$  [28]. However, the overall effect of  $P_{ex}$  on the electron neutrino flux at the detector is modified by the factor  $r \cos^2 \theta_{23} - 1$  as seen in Eq. (5). Since the atmospheric neutrino flux ratio is  $r \sim 2$  at low energies, there is no change in the  $\nu_e$  flux if  $r \cos^2 \theta_{23} = 1$  ( $\theta_{23} = \pi/4$ ). If  $\cos^2 \theta_{23}$  is greater (less) than 0.5 ( $\theta_{23} < (>) \pi/4$ ) there is an expected enhancement (reduction) of the flux. Therefore it may be possible to determine the octant of  $\theta_{23}$  by observing changes in the flux of the low energy electronlike ( $e$ -like) samples at SK. Analogous changes to the  $\nu_\mu$  flux on the other hand are suppressed by the leading factor of  $1/r$  in the second term of Eq. (5). Further, vacuum oscillations of the low energy  $\nu_\mu$  flux are already well averaged so the correction appearing in the third term is negligible. The expected change in the  $\nu_e$  flux as a function of energy and zenith angle for different values of  $\theta_{23}$  is shown as the right panel of Fig. 1.

When  $\theta_{13}$  is different from zero, the matrix  $U_{13}$  is no longer sufficiently close to unity, and the above relations do not hold. Instead, in the search for nonzero  $\theta_{13}$ , the oscillation analysis is done using a ‘‘one mass scale dominant’’ scheme wherein the solar neutrino mass difference is taken

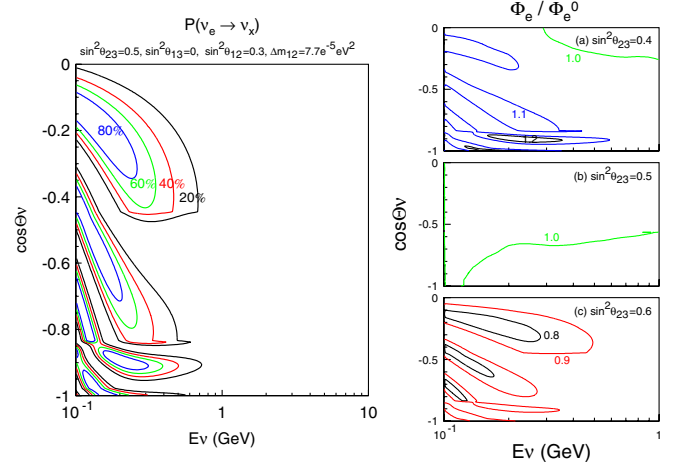


FIG. 1 (color online). The left side of the figure shows the calculated  $\nu_e$  transition probability  $P_{ex}$  for atmospheric neutrinos with an energy  $E_\nu$  and neutrino zenith angle,  $\cos \Theta_\nu$ , using  $\Delta m_{12}^2 = 7.7 \times 10^{-5} \text{ eV}^2$ ,  $\sin^2 \theta_{12} = 0.3$  [28],  $\sin^2 \theta_{23} = 0.5$ ,  $\sin^2 \theta_{13} = 0.0$  and  $\Delta m_{23}^2 = 2.1 \times 10^{-3} \text{ eV}^2$ . Matter effects within the Earth are taken into account. Negative  $\cos \Theta_\nu$  corresponds to upward-going neutrinos and 0 is the horizon. The electron neutrino flux ratio  $\Phi_e / \Phi_e^0$  is shown in the right side of the figure. An expected excess (deficit) for atmospheric mixing in the first (second) octant is shown in the upper (lower) panel. The island shapes are regions of probability driven by the solar oscillation parameters. The center panel shows no significant region of excess or deficit when  $\sin^2 \theta_{23} = 0.5$ .

to be much smaller than the atmospheric mass difference. Accordingly, the solar mass difference is neglected and a single mass splitting is adopted,  $\Delta m^2 \equiv m_3^2 - m_{1,2}^2$  such that  $\Delta m^2 > 0$  ( $\Delta m^2 < 0$ ) corresponds to the normal (inverted) mass hierarchy. In vacuum,

$$P(\nu_e \rightarrow \nu_e) = 1 - \sin^2 2\theta_{13} \sin^2 \left( \frac{1.27 \Delta m^2 L}{E} \right)$$

$$P(\nu_\mu \leftrightarrow \nu_e) = \sin^2 \theta_{23} \sin^2 2\theta_{13} \sin^2 \left( \frac{1.27 \Delta m^2 L}{E} \right)$$

$$P(\nu_\mu \rightarrow \nu_\mu) = 1 - 4 \cos^2 \theta_{13} \sin^2 2\theta_{23} (1 - \cos^2 \theta_{13} \sin^2 2\theta_{23}) \times \sin^2 \left( \frac{1.27 \Delta m^2 L}{E} \right). \quad (6)$$

Under this framework the three-neutrino oscillation probability in constant density matter may be written [29] as

$$P(\nu_\mu \leftrightarrow \nu_e) = \sin^2 \theta_{23} \sin^2 2\theta_{13}^M \sin^2 \left( \frac{1.27 \Delta m_{M}^2 L}{E} \right). \quad (7)$$

The matter modified mixing parameters are

$$\Delta m_M^2 = \Delta m^2 \sqrt{\sin^2 2\theta_{13} + (\Gamma - \cos 2\theta_{13})^2}$$

$$\sin^2 2\theta_{13}^M = \frac{\sin^2 2\theta_{13}}{\sin^2 2\theta_{13} + (\Gamma - \cos 2\theta_{13})^2}, \quad (8)$$

where  $\Gamma = \pm 2\sqrt{2}G_f n_e E / \Delta m^2$ ,  $G_f$  is the Fermi constant,  $n_e$  is the local electron density, and the plus (minus) sign specifies neutrinos (antineutrinos). Resonant enhancement of the oscillation probability occurs when  $|\Gamma| = \cos 2\theta_{13}$  and holds for either neutrinos or antineutrinos, depending on the mass hierarchy. Further, when  $\theta_{13} = 0$  there is no enhancement.

Oscillation probabilities for neutrinos traversing the Earth appear in the left panel of Fig. 2. For  $\Delta m^2 \sim 2 \times 10^{-3} \text{ eV}^2$  this resonance occurs in the 2–10 GeV region and its strength increases with  $\theta_{13}$  reaching  $\sim 40\%$  conversion probability near the Chooz limit. Under these conditions, the primary signature in the atmospheric neutrino sample at Super-K is an increased rate of high energy upward-going  $e$ -like events. The right panel of the figure shows the  $\nu_e$  flux ratio at SK oscillated with  $\theta_{13}$  at the Chooz limit relative to that oscillated at  $\theta_{13} = 0$ . Additional  $\theta_{13}$ -induced effects on muon event rates are expected, but are generally much smaller. For large values of  $\theta_{13}$  an expected  $\sim 20\%$  increase in the multiring  $e$ -like event (see below) rate would be accompanied by a  $\sim 5\%$  change in similarly energetic muonlike ( $\mu$ -like) samples.

Including solar oscillation terms changes the oscillation probability in the resonance region by less than 5%, supporting our assumption of the “one mass scale dominant” framework. Their inclusion as an additional scanning parameter also introduces a large computational burden in the  $\theta_{13}$  analysis and further motivates a separate  $\theta_{23}$  octant analysis.

Oscillation probabilities in both analyses are computed using a numerical technique [30]. Probabilities inside the Earth are computed using a piecewise constant radial matter density profile constructed as the median density in each of the dominant regions of the preliminary reference Earth model (PREM) [31]: inner core ( $0 \leq r < 1220 \text{ km}$ )  $13.0 \text{ g/cm}^3$ , outer core ( $1220 \leq r < 3480 \text{ km}$ )  $11.3 \text{ g/cm}^3$ , mantle ( $3480 \leq r < 5701 \text{ km}$ )  $5.0 \text{ g/cm}^3$ , and the crust ( $5701 \leq r < 6371 \text{ km}$ )  $3.3 \text{ g/cm}^3$ . Transition amplitudes are computed across each layer a neutrino traverses and the product of these together with the amplitude for crossing the Earth’s atmosphere is used to compute the final oscillation probability. The difference in the obtained probabilities using this simplified model compared to the more expansive PREM model have a negligible impact on the final analysis results after incorporating detector resolution effects.

### III. DATA SAMPLE

Super-Kamiokande is a cylindrical 50 kton water Cherenkov detector situated at a depth of 2700 meters water equivalent. The detector volume is optically separated into an inner volume (ID) and an outer veto region (OD). During the SK-I (SK-II) periods the ID was instrumented with 11 146 (5182) inward-facing 20-inch photomultiplier tubes (PMTs) and the OD with 1885 outward-facing 8-inch PMTs. In SK-III there were 11 129 ID PMTs. Since SK-II, the ID PMTs have been encased in fiber-reinforced plastic shells with acrylic covers to prevent chain reactions within the detector in the event of a PMT implosion. A more detailed description of the detector may be found in [32].

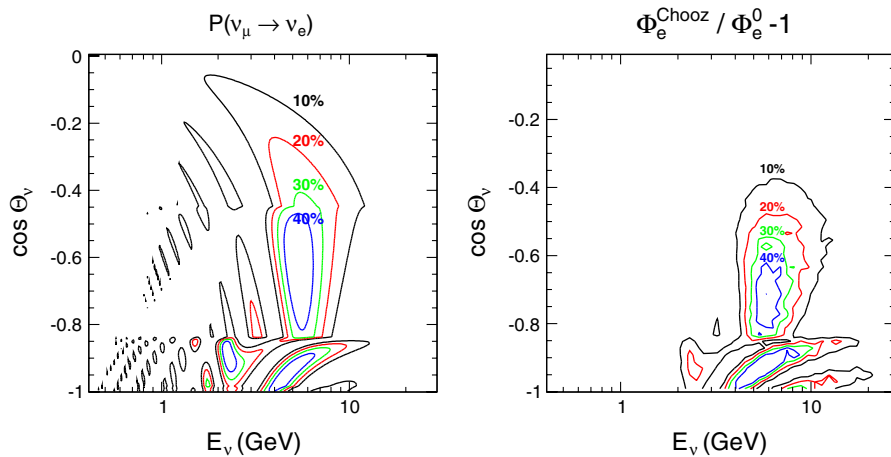


FIG. 2 (color online). The three flavor oscillation probability  $\nu_\mu \leftrightarrow \nu_e$  for  $\theta_{13}$  at the Chooz limit for neutrinos under the normal hierarchy in the one mass scale dominant framework is shown at left. In the right panel the  $\nu_e$  flux ratio  $\Phi_e^{\text{Chooz}} / \Phi_e^0 - 1$  for oscillations with  $\theta_{13}$  at the Chooz limit relative to those at  $\theta_{13} = 0$ . Large matter-induced resonances between 2–10 GeV appear for upward-going neutrinos traversing the core ( $\cos \Theta_\nu < -0.84$ ) and mantle regions ( $-0.84 < \cos \Theta_\nu < -0.45$ ). Atmospheric mixing is assumed at  $\Delta m_{23}^2 = 2.1 \times 10^{-3} \text{ eV}^2$  and  $\sin^2 \theta_{23} = 0.5$ .

In this paper, atmospheric neutrino events are organized into three classes: fully contained (FC), partially contained (PC), and upward-going muons ( $UP\mu$ ). Events which deposit all of their Cherenkov light in the ID are classified as FC, while events that originate in the ID but have an exiting particle depositing energy in the OD are considered PC. Neutrino interactions occurring in the rock beneath the detector which produce muons that traverse the detector (through-going) or stop in the detector (stopping) are classified as  $UP\mu$  events. Data accrued in the five years spanning the SK-I run period starting in 1996 correspond to 1489 live days of FC and PC events with 1646  $UP\mu$  live days. SK-II data were taken between December 2002 and October 2005 and represent 799 (518) live days of FC and PC events and 828 live days of  $UP\mu$  events. SK-III data were taken between December 2005 and June 2007 where the FC and PC live time was 518 days and that for  $UP\mu$  was 635. The difference of live times between FC/PC and  $UP\mu$  is due to the insensitivity of the  $UP\mu$  reduction to noise such as “flasher” PMTs. Such noise may be misconstructed as real FC/PC events so in those reductions data surrounding these events are rejected.

Fully contained events are further divided into sub-GeV and multi-GeV subsamples based on visible energy,  $E_{vis}$ . Events with  $E_{vis} < 1.33$  GeV are considered sub-GeV. The number of reconstructed Cherenkov rings in an event is also used to separate these samples into single- and multiring subsamples. Single-ring events are classified into  $\mu$ -like and  $e$ -like samples by the ring pattern. For multiring samples, the most energetic ring is used to classify the event type. Partially contained events are classified as “OD stopping” or “OD through-going” based on their energy deposition in the OD [33]. Similarly,  $UP\mu$  events that traverse the detector are separated into “showering” and “nonshowering” based on the method described in [34] while those that enter and stop within the detector are classified as “stopping.” These samples are defined for all of the SK run periods. To enhance each analysis’ sensitivity to the desired oscillation effect, the FC samples have been further divided as outlined below. However, all of the data samples are used in both analyses.

Several improvements to the reconstruction and Monte Carlo (MC) since earlier publications [10,11] are incorporated in this paper. The ring counting likelihood has been updated to improve separation between the single-ring and multiring samples. Additionally, the neutrino interaction generator has been updated to include lepton mass effects in charged-current (CC) interactions [35,36]. An axial vector mass of 1.2 GeV has been used for quasi-elastic and single meson production processes and cross sections for deep inelastic scattering are computed based on the GRV98 parton distribution functions [37]. The atmospheric neutrino flux is taken from [38]. More detailed information on the MC simulation, event generator, and event reconstruction is presented in [11].

### A. Additional sample selection for the $\theta_{23}$ octant analysis

To increase the purity of the interaction mode, FC sub-GeV single-ring events are separated into subsamples based on their number of decay electrons and how  $\pi^0$ -like they are.

The FC sub-GeV single-ring  $e$ -like sample contains background events which are mainly neutral-current (NC)  $\pi^0$  events where one of the two  $\gamma$  rays from the  $\pi^0$  decay has been missed by the event reconstruction. The electromagnetic shower from the  $\gamma$  gives a light pattern similar to that of an electron and results in an electronlike classification. To reduce this type of background, a specialized  $\pi^0$  fitter is used [39]. This fitter enforces a second ring on the data and then predicts a light pattern that would result from  $\gamma$  rays propagating through the tank with the direction and vertex of the fitted rings. The intensity of each fitted ring as well as its direction are varied until the predicted light pattern best agrees with the observed one. Since the interaction mode of interest, charged-current quasielastic (CCQE), creates only one light-emitting particle, constructing the invariant mass for the two fitted rings provides some separation between CCQE and NC events. The left five panels in Fig. 3 show the invariant mass distributions from this  $\pi^0$  fitter for CCQE and NC events in the FC sub-GeV single-ring  $e$ -like Monte Carlo in five energy regions. Neutral-current events tend to form a peak close to the  $\pi^0$  mass whereas CCQE events do not. For events with electron momentum below 250 MeV/c, a cut at 100 MeV/c<sup>2</sup> is used to create a  $\pi^0$ -like sample. This cut, however, is not sufficient for higher electron momenta so an additional likelihood selection is used, incorporating three variables: the  $\pi^0$  invariant mass distribution, the fraction of the event’s reconstructed momentum carried by the second ring, and the difference of two likelihood variables which result from a  $\pi^0$ -fit and electron-fit. The distribution of these variables is shown in Fig. 3. The  $\pi^0$ -like selection likelihood functions are defined as

$$\mathcal{L} = \sum_{i=1}^3 \log(\Gamma_i^S(x_i)) - \log(\Gamma_i^B(x_i)), \quad (9)$$

where  $\Gamma_i^S(x_i)$  ( $\Gamma_i^B(x_i)$ ) represents the CCQE(NC) events’ probability distribution function (PDF) for the  $i$ th variable with observable  $x_i$ .

After separating the  $\pi^0$ -like sample, the remaining  $e$ -like events are divided into two categories, 0-decay which has no decay electrons and 1-decay which has one or more decay electrons. Since  $\nu_e$  CCQE events are not expected to produce decay electrons, there is a large fraction of CCQE interactions in the 0-decay sample. For the FC sub-GeV single-ring  $\mu$ -like sample, there are three categories using the number of decay electrons: 0-decay, 1-decay, and 2-decay, corresponding to the number of decay electrons reconstructed in the event. Since these

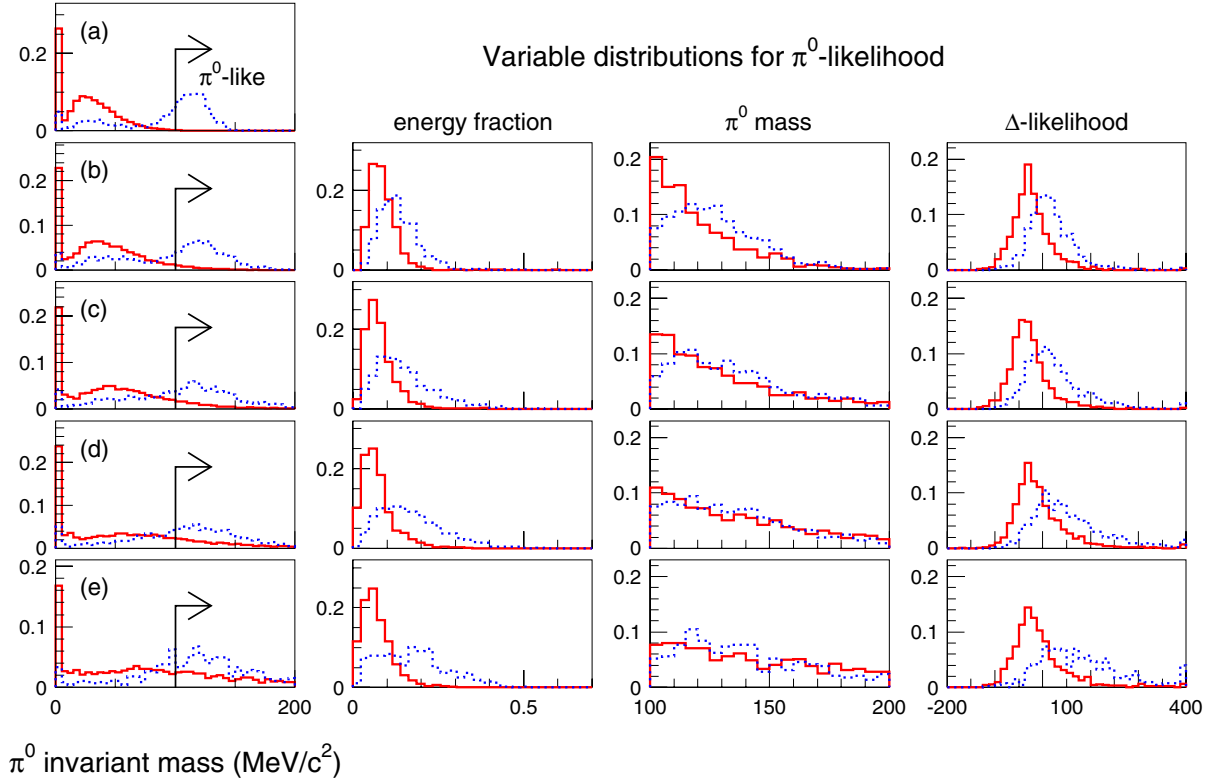


FIG. 3 (color online). The distributions used in the  $\pi^0$  selection for five momentum regions: (a)  $P_e < 250$  MeV/ $c$ , (b)  $250$  MeV/ $c \leq P_e < 400$  MeV/ $c$ , (c)  $400$  MeV/ $c \leq P_e < 630$  MeV/ $c$ , (d)  $630$  MeV/ $c \leq P_e < 1000$  MeV/ $c$ , and (e)  $1000$  MeV/ $c \leq P_e$ . Solid (dashed) lines represent CCQE (NC) events in the FC sub-GeV single-ring  $e$ -like Monte Carlo. Events with an invariant mass above  $100$  MeV/ $c^2$  are selected as  $\pi^0$ -like. To separate  $\pi^0$ -like and electronlike more efficiently, an additional likelihood selection is applied for events with momentum above  $250$  MeV/ $c$ . The distributions of the three likelihood variables are shown: the fraction of energy carried by the second fitted ring [ $E_2/(E_1 + E_2)$ ], the  $\pi^0$  mass, and  $\Delta$ -likelihood (described in the text). All distributions have been normalized to unit area.

TABLE I. The number of FC sub-GeV MC events and their fractional composition by neutrino interaction mode in SK-I. The upper (lower) table shows the  $e$ -like ( $\mu$ -like) sample. The left (right) side of the table shows the result after (before) separation into subsamples. After separation, the CCQE purity is increased and the NC backgrounds are reduced in the 0-decay  $e$ -like and 1-decay  $\mu$ -like subsamples.

		FC sub-GeV single-ring $e$ -like			FC sub-GeV single-ring $e$ -like
		0-decay	1-decay	$\pi^0$ -like	
MC events		2663.2	210.9	191.8	2996.4
	QE	77.7%	3.8%	10.6%	70.6%
CC	single meson	12.4%	50.3%	7.0%	15.2%
$\nu_e + \bar{\nu}_e$	multi $\pi$	1.0%	9.7%	1.8%	1.7%
	coherent $\pi$	1.3%	8.5%	0.5%	1.7%
CC $\nu_\mu + \bar{\nu}_\mu$		0.6%	15.2%	7.0%	2.0%
NC		6.8%	11.2%	72.0%	8.7%
		FC sub-GeV single-ring $\mu$ -like			FC sub-GeV single-ring $\mu$ -like
		0-decay	1-decay	2-decay	
MC events		1412.4	2745.4	164.3	4297.8
	QE	71.3%	78.5%	5.8%	74.7%
CC	single meson	12.9%	15.5%	65.7%	16.7%
$\nu_\mu + \bar{\nu}_\mu$	multi $\pi$	1.1%	1.5%	14.9%	1.9%
	coherent $\pi$	0.8%	1.5%	8.6%	1.6%
CC $\nu_e + \bar{\nu}_e$		1.8%	<0.1%	<0.1%	0.7%
NC		11.8%	2.6%	3.3%	4.3%

CCQE events produce a muon they are expected to have at least one decay electron. Details of the event composition by interaction mode after these event selections are shown in Table I. The fraction of CCQE events is increased in the 0-decay  $e$ -like and 1-decay  $\mu$ -like samples so they should improve sensitivity to changes in the sub-GeV flux induced by solar oscillations.

### B. Additional sample selection for the $\theta_{13}$ analysis

To improve sensitivity to  $\nu_e$  appearance induced by nonzero  $\theta_{13}$ , an enhanced FC multi-GeV multiring electronlike sample is created. The selection is based on a likelihood method [10] for SK-I and is extended in this analysis to SK-II and SK-III. The likelihood functions have been rebuilt using 100 years of MC incorporating recent improvements to the SK event reconstruction. Accordingly, the event populations of the SK-I sample here differ from those in the reference.

The MC is divided into five energy bins, 1.33–2.5 GeV, 2.5–5 GeV, 5–10 GeV, 10–20 GeV, and >20 GeV and PDFs for each bin are constructed using events whose most energetic ring has been reconstructed as electronlike. Four observables are used in the event selection: the number of decay electrons in the event, the maximum distance between the neutrino vertex and any muon decay electrons, the fraction of momentum carried by the event's most energetic ring, and the particle identification (PID) likelihood value of that ring. The final likelihood functions are defined as

$$\mathcal{L}_j = \sum_{i=1}^4 \log(\Gamma_i^S(x_i)) - \log(\Gamma_i^B(x_i)), \quad (10)$$

where  $\Gamma_i$  represents the PDF for the  $i$ th observable and  $x_i$  is the observable's measured value. The superscripts  $S$  and  $B$  label the signal and background PDFs, respectively. The

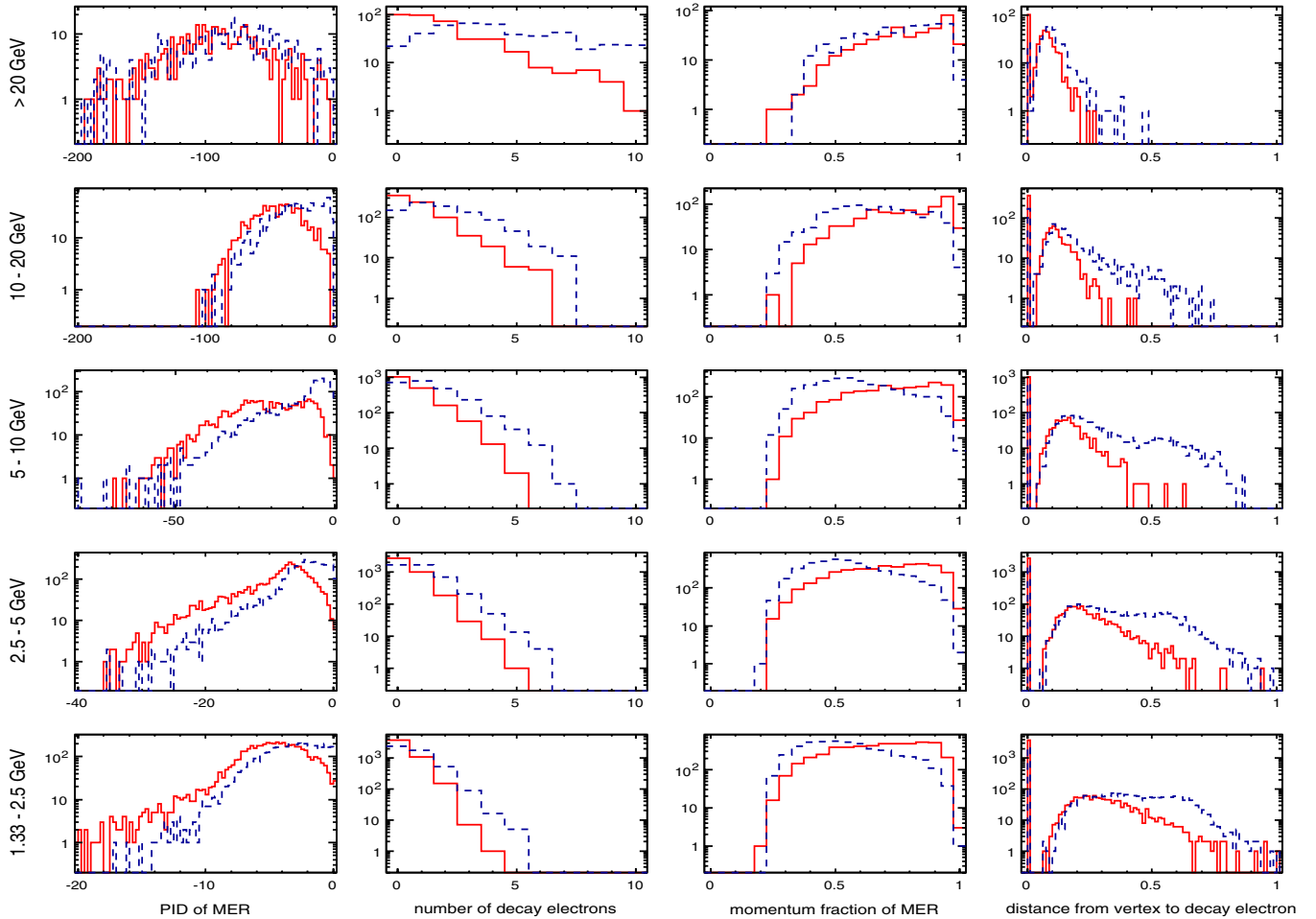


FIG. 4 (color online). Variables used in the likelihood definition to create the SK-I multi-GeV multiring  $e$ -like sample. The energy bins correspond to the most energetic ring (MER) and the distributions have been scaled to the SK-I live time. Signal events (CC  $\nu_e + \bar{\nu}_e$ ) are shown as the solid line and background events (CC  $\nu_\mu + \bar{\nu}_\mu$  and NC) are shown as the dashed line. The shapes of these distributions do not differ appreciably among SK-I, SK-II, and SK-III.

TABLE II. The expected number of events for each interaction component of the multiring multi-GeV  $e$ -like sample before (No  $\mathcal{L}$ ) and after ( $\mathcal{L}$ ) likelihood selection for the SK-I, SK-II, and SK-III MC scaled to 1489, 798, and 518 live time days, respectively. Two flavor neutrino oscillations  $\nu_\mu \leftrightarrow \nu_\tau$  have been assumed with  $\Delta m^2 = 2.1 \times 10^{-3} \text{ eV}^2$  and  $\sin^2 2\theta = 1.0$ .

	CC $\nu_e + \bar{\nu}_e$		CC $\nu_\mu + \bar{\nu}_\mu$		NC		Total	
	No $\mathcal{L}$	$\mathcal{L}$	No $\mathcal{L}$	$\mathcal{L}$	No $\mathcal{L}$	$\mathcal{L}$	No $\mathcal{L}$	$\mathcal{L}$
SK-I	472.1	331.0	201.7	39.2	218.1	74.4	891.9	444.6
Percentage (%)	53.0	74.5	22.6	8.8	24.5	16.7	100.0	100.0
SK-II	253.4	178.0	110.7	23.4	119.1	42.8	483.2	244.2
Percentage (%)	52.4	72.9	23.0	9.6	24.6	17.5	100.0	100.0
SK-III	157.6	112.8	72.7	15.1	74.0	26.1	304.3	154.0
Percentage (%)	51.8	73.2	23.9	9.8	24.3	17.0	100.0	100.0

index  $j$  specifies the likelihood corresponding to one of the five energy bins considered. In selecting electron neutrino events, the signal is taken to be CC  $\nu_e + \bar{\nu}_e$ , while the background is composed of both CC  $\nu_\mu + \bar{\nu}_\mu$  and NC

events. An event makes it into the final multi-GeV multiring sample if it passes all cuts in the FC reduction, if the event's most energetic ring is electronlike, and if  $\mathcal{L}_j > 0$ . Distributions of the likelihood variables for signal and

TABLE III. Summary of atmospheric neutrino data and MC event samples for FC, PC, and UP $\mu$  in SK-I, SK-II, and SK-III. The FC and PC live time is 1489 days in SK-I, 798 days in SK-II, and 518 days in SK-III. The live time of the UP $\mu$  samples is 1645 days in SK-I, 827 days in SK-II, and 635 days in SK-III. The number of MC events has been normalized by the live time of the data. The oscillated MC has been calculated using two flavor mixing at  $\Delta m^2 = 2.1 \times 10^{-3} \text{ eV}^2$  and  $\sin 2\theta = 1.0$ .

	Data	SK-I MC	(osc.)	Data	SK-II MC	(osc.)	Data	SK-III MC	(osc.)
FC sub-GeV									
single-ring									
$e$ -like									
0-decay	2984	2655.9	(2652.4)	1605	1405.8	(1403.4)	1098	935.7	(934.7)
1-decay	275	204.4	(194.3)	155	113.5	(107.1)	106	69.6	(66.7)
$\pi^0$ -like	167	159.1	(155.2)	81	81.3	(79.1)	46	45.6	(44.4)
$\mu$ -like									
0-decay	1036	1385.6	(973.0)	563	765.9	(537.2)	346	497.5	(350.4)
1-decay	2035	2760.6	(1846.8)	1043	1429.4	(957.3)	759	999.8	(668.3)
2-decay	150	163.7	(114.6)	80	82.8	(57.7)	61	58.5	(41.0)
2-ring $\pi^0$ -like	497	460.0	(456.1)	267	237.3	(235.1)	178	157.8	(156.5)
FC multi-GeV									
single-ring									
$e$ -like	829	777.8	(777.7)	392	409.9	(411.1)	282	279.3	(278.4)
$\mu$ -like	694	1027.4	(744.4)	394	550.2	(399.0)	231	352.8	(255.7)
multiring									
$e$ -like	433	457.9	(458.9)	260	252.3	(251.9)	149	159.2	(159.1)
$\mu$ -like	617	882.4	(660.9)	361	459.6	(344.1)	226	313.8	(234.4)
PC									
OD stopping	163	222.7	(167.3)	116	105.8	(80.9)	63	75.1	(55.7)
OD through-going	735	965.4	(755.0)	314	482.5	(374.7)	280	334.9	(262.8)
Upward-going muon									
stopping	435.9	701.7	(419.4)	207.6	355.2	(212.5)	193.7	273.8	(163.5)
nonshowering	1577.4	1548.0	(1343.9)	725.3	767.6	(668.7)	612.9	599.4	(520.0)
showering	271.6	302.7	(292.2)	108.1	147.8	(143.6)	110	116.2	(112.3)
Reduction efficiency									
FC			97.6%			99.2%			98.5%
PC			81.0%			74.8%			88.6%
Upward-stopping $\mu$			98.0%			97.0%			98.2%
Upward through-going $\mu$			99.4%			98.1%			99.4%

background events appear in Fig. 4. Decay electrons are produced in the signal sample through the decay chain of pions produced in these events. However, lacking an exiting muon at the interaction vertex, fewer decay electrons are expected in the signal sample. Similarly, the maximum distance to a decay electron in the CC component of the background is expected to be larger due to the presence of energetic muons. The distribution of the momentum fraction carried by the most energetic ring tends to peak toward higher values for signal events where the outgoing electron has been correctly identified as electronlike. Background events, on the other hand, tend to peak at lower momentum fractions where the most energetic ring comes from a meson or muon that has been misidentified as electronlike. Applying the likelihood improves the signal purity from 53% to 74% in SK-I with 16% of the sample coming from NC events. Table II shows the event compositions of the multi-GeV  $e$ -like sample after this selection for SK-I, SK-II, and SK-III.

A summary of all atmospheric neutrino event samples used in this paper is shown in Table III.

#### IV. OSCILLATION ANALYSIS

The oscillation analyses have been performed using the above data samples. Since the physical detector configuration differs between SK-I, SK-II, and SK-III, separate 500-years-equivalent MC data sets for each run period are used. The data are compared against the MC expectation using a ‘‘pulled’’  $\chi^2$  [40] method based a Poisson probability distribution:

$$\chi^2 = 2 \sum_n \left( E_n \left( 1 + \sum_i f_n^i \epsilon_i \right) - \mathcal{O}_n + \mathcal{O}_n \ln \frac{\mathcal{O}_n}{E_n (1 + \sum_i f_n^i \epsilon_i)} \right) + \sum_i \left( \frac{\epsilon_i}{\sigma_i} \right)^2, \quad (11)$$

where  $n$  indexes the data bins,  $E_n$  is the MC expectation, and  $\mathcal{O}_n$  is the number of observed events in the  $n$ th bin. Systematic errors are incorporated into the fit via the systematic error parameter  $\epsilon_i$ , where  $i$  is the systematic error index and  $f_n^i$  is the fractional change in the MC expectation in bin  $n$  for a  $1\text{-}\sigma$  change in the  $i$ th systematic error. The  $1\text{-}\sigma$  value of a systematic error is labeled as  $\sigma_i$ . Equation (11) is minimized with respect to the  $\epsilon_i$  at each point in a fit’s oscillation parameter space according to  $\frac{\partial \chi^2}{\partial \epsilon_i} = 0$ . This derivative yields a set of linear equations in  $\epsilon$  that can be solved iteratively [40]. The best-fit point is defined as the global minimum  $\chi^2$  on the grid of oscillation points.

To ensure stability of the function in Eq. (11) the binning has been chosen so that there are at least 6 expected MC events in each bin after scaling to the SK-I live time. Data are binned separately for SK-I, SK-II, and SK-III, each

with a total of 420 bins. Both analyses simultaneously fit 16 event samples, including both  $e$ -like and  $\mu$ -like event categories, shown in Table III. The samples separated by number of decay electrons are divided into 5 momentum and 10 zenith angle bins for the 0-decay  $e$ -like, 0-decay and 1-decay  $\mu$ -like samples, and 1 zenith bin otherwise. The remaining FC events are divided among 14 momentum bins, PC events into a total of 6 bins, and all upward through-going muon samples have one momentum bin each. The upward-stopping muon samples have been divided into three momentum bins. All of these samples are further divided into 10 evenly spaced zenith angle bins. FC and PC events range from  $-1 \leq \cos\Theta \leq 1$  and UP $\mu$  events are binned from  $-1 \leq \cos\Theta \leq 0$ .

Both analyses consider 120 sources of systematic uncertainty. These systematic errors are separated into two categories, those that are common to all of the SK run periods and those that differ. Errors that are classified as common are related to uncertainties in the atmospheric neutrino flux, neutrino interaction cross sections, and particle production within nuclei. Systematic errors that are independent for SK-I, SK-II, and SK-III represent uncertainties related to the detector performance in each era. Particle reconstruction and identification uncertainties, as well as energy scale and fiducial volume uncertainties, differ for SK-I, SK-II, and SK-III because of their different geometries. These systematics are therefore considered as separate sources of uncertainty. The effects of the systematic uncertainties are introduced by the coefficients  $f_n^i$  which are computed for every bin and error in the analysis. For common systematic uncertainties there is a coefficient for every bin in the analysis. On the other hand, indepen-

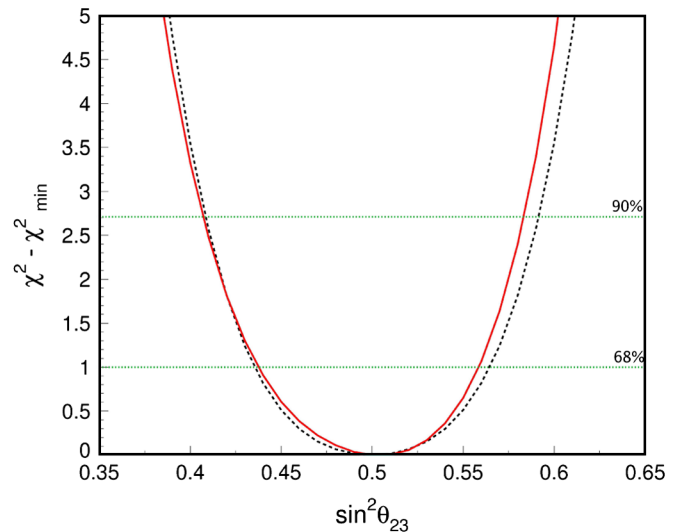


FIG. 5 (color online).  $\chi^2 - \chi_{\min}^2$  distribution as a function of  $\sin^2\theta_{23}$  for oscillations without the 1–2 parameters (dotted line) and with the 1–2 parameters (solid line). For each  $\sin^2\theta_{23}$  point,  $\Delta m_{23}^2$  is chosen so that  $\chi^2$  is minimized. The horizontal line corresponds to the 68% (90%) confidence level which is located at  $\chi_{\min}^2 + 1.0(2.7)$ .

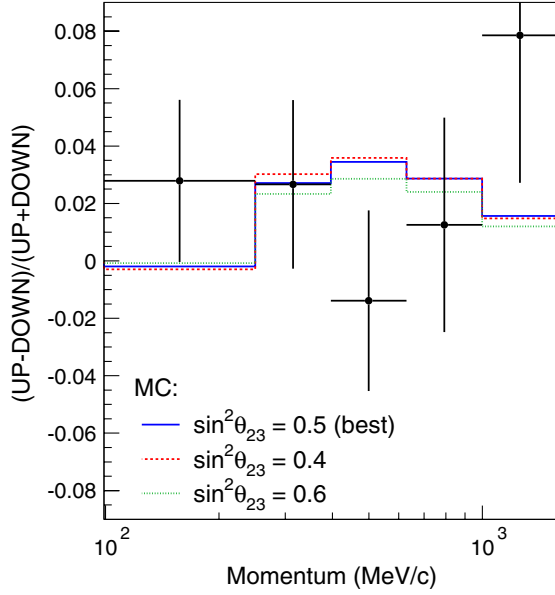


FIG. 6 (color online). Asymmetry (up – down)/(up + down) for the SK-I + II + III single-ring  $e$ -like 0-decay data set in the octant analysis. Up is defined as events with  $\cos\Theta < -0.2$  and down as  $\cos\Theta > 0.2$ . The solid line represents the MC expectation at the best-fit point and the dashed (dotted) line shows the expected asymmetry for  $\sin^2\theta_{23} = 0.4(0.6)$ . The error bars are statistical.

dent systematic errors specific to SK-I (II, III) have non-zero coefficients for the SK-I (II, III) analysis bins and are zero otherwise. Tables V and VI list the 33 common errors separated into neutrino flux and interaction-related systematics, respectively. Table VII lists the  $29 \times 3$  independent systematic errors and all three tables show errors with their fitted value,  $\epsilon_i$ , from the  $\theta_{13}$  search, together with their uncertainty. More information about these systematic errors is presented in a previous analysis [11].

To prevent instabilities in the  $\chi^2$  value resulting from the low statistics data in later SK run periods, the SK-II and SK-III bins are merged with those of SK-I. In the minimization of the function in Eq. (11) the following changes are made:

$$\mathcal{O}_n \rightarrow \sum_i \mathcal{O}_n^{SKi}$$

$$E_n \left( 1 + \sum_j f_n^j \epsilon_j \right) \rightarrow \sum_i E_n^{SKi} \left( 1 + \sum_j f_n^j \epsilon_j \right).$$

TABLE IV. Best-fit information for fits to the SK-I + II + III data for both hierarchies in the  $\theta_{13}$  analysis. The limit on  $\sin^2\theta_{13}$  is the C.L. in one dimension at 90% and the corresponding bounds on  $\Delta m^2$  are  $1.9(1.7) \times 10^{-3} < \Delta m^2 < 2.6(2.7) \times 10^{-3} \text{ eV}^2$  in the normal (inverted) hierarchy.

SK-I + II + III	$\sin^2\theta_{13}$ 90% C.L.	$\sin^2\theta_{13}$	$\Delta m^2$ [eV <sup>2</sup> ]	$\sin^2\theta_{23}$	$\chi^2$ /d.o.f.
Normal hierarchy	<0.04	0.00	$2.1 \times 10^{-3}$	0.50	468.7/417
Inverted hierarchy	<0.09	0.006	$2.1 \times 10^{-3}$	0.53	468.4/417

Since the systematic error coefficients are computed for separate SK-I, SK-II, and SK-III bins as discussed above, merging in this way preserves the effect of the systematic errors specific to each detector geometry. Using this method, the final  $\chi^2$  is taken over 420 merged bins.

### A. $\theta_{23}$ octant analysis

In the search for  $\theta_{23} \neq \pi/4$ , two fits are performed to the data to extract a constraint on  $\sin^2\theta_{23}$  assuming  $\theta_{13} = 0$ . The first (solar-off) is done over the two-dimensional space of  $\Delta m_{23}^2$  and  $\sin^2\theta_{23}$  (41 points each of  $\Delta m_{23}^2$  in  $[1.0, 6.3] \times 10^{-3} \text{ eV}^2$  and  $\sin^2\theta_{23}$  in  $[0.3, 0.7]$ ) and is compared to a second (solar-on) fit, expanded to four dimensions including the solar oscillation parameters  $\Delta m_{12}^2$  and  $\sin^2\theta_{12}$  (fit over 4 points of  $\Delta m_{12}^2$  in  $[7.41, 7.94] \times 10^{-5} \text{ eV}^2$  and 5 points of  $\sin^2\theta_{12}$  in  $[0.28, 0.36]$ ). This grid of points has been chosen based on a combined fit of the solar neutrino experiment and KamLAND data [28,46]. To constrain the fit over the solar parameters, the  $\Delta\chi_{\text{solar}}^2$  value from this combined analysis is then added to that of the fit at each of these grid points.

Figure 5 shows the  $\Delta\chi^2$  distributions with and without the solar parameters as a function of  $\sin^2\theta_{23}$ , where  $\Delta m_{12}^2$ ,  $\Delta m_{23}^2$ , and  $\sin^2\theta_{12}$  are chosen so that  $\chi^2$  is minimized. The best-fit point with the solar parameters is located at  $\sin^2\theta_{23} = 0.50$ ,  $\Delta m_{23}^2 = 2.1 \times 10^{-3} \text{ eV}^2$ ,  $\sin^2\theta_{12} = 0.30$ , and  $\Delta m_{12}^2 = 7.59 \times 10^{-5} \text{ eV}^2$ , with a minimum  $\chi^2$  of 470.6/416 d.o.f., while that without the solar parameters is  $\sin^2\theta_{23} = 0.50$ ,  $\Delta m_{23}^2 = 2.1 \times 10^{-3} \text{ eV}^2$ , with a minimum  $\chi^2$  of 469.6/418 d.o.f. No significant deviation of  $\sin^2\theta_{23}$  from  $\pi/4$  is seen with the addition of solar terms to the analysis but they do give rise to the asymmetric shape seen in the  $\chi^2$  distribution. Including the solar terms constrains the measurement of  $\sin^2\theta_{23}$  at the 68 (90)% C.L. to  $0.438(0.407) < \sin^2\theta_{23} < 0.558(0.583)$ . The up-down asymmetry of the single-ring  $e$ -like data in comparison with the best-fit MC expectation and the expectations for  $\sin^2\theta_{23} = 0.4$  and  $0.6$  appears in Fig. 6.

### B. $\theta_{13}$ analysis

In the  $\theta_{13}$  analysis, oscillation fits are performed by scanning a grid of 83 025 oscillation points in three variables:  $\log\Delta m^2$ ,  $\sin^2\theta_{23}$ , and  $\sin^2\theta_{13}$ . The fitting procedure has been performed on the combined SK-I + II + III data set assuming both a normal and inverted hierarchy. The

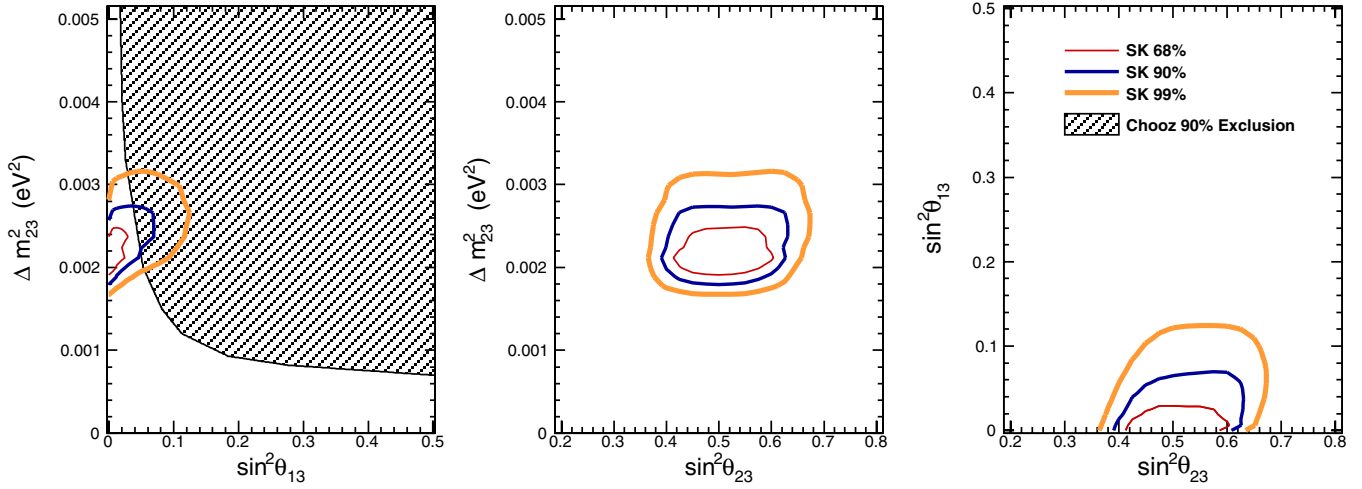


FIG. 7 (color online). Normal hierarchy allowed regions at 68% (thin line), 90% (medium line), and 99% (thick line) C.L. for the SK-I + II + III data. The shaded region in the first panel shows the Chooz 90% exclusion region.

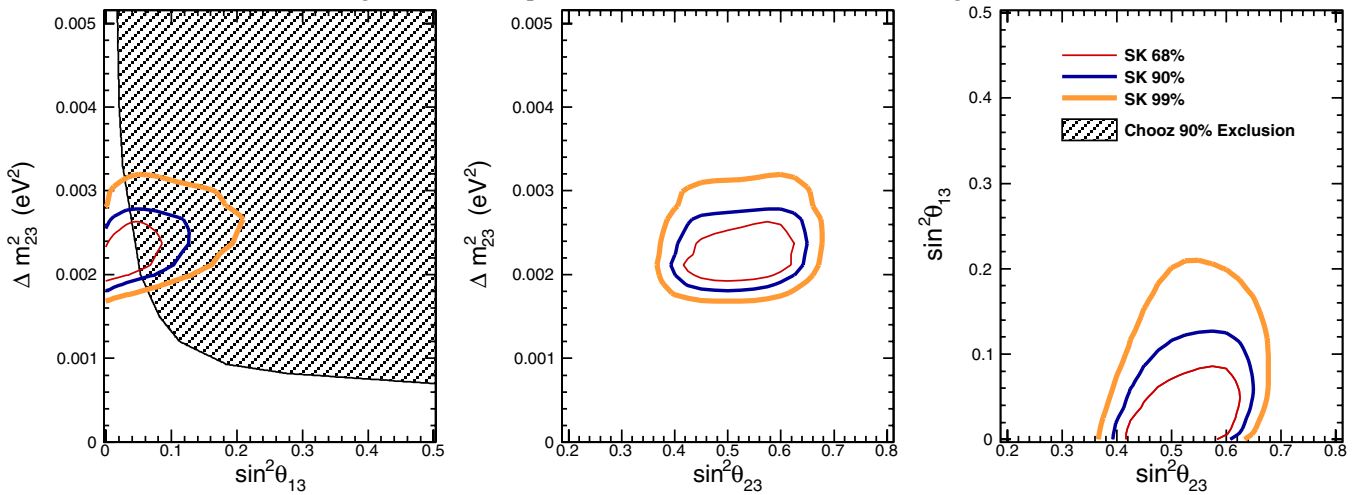


FIG. 8 (color online). Inverted hierarchy allowed regions at 68% (thin line), 90% (medium line), and 99% (thick line) C.L. for the SK-I + II + III data. The shaded region in the first panel shows the Chooz 90% exclusion region.

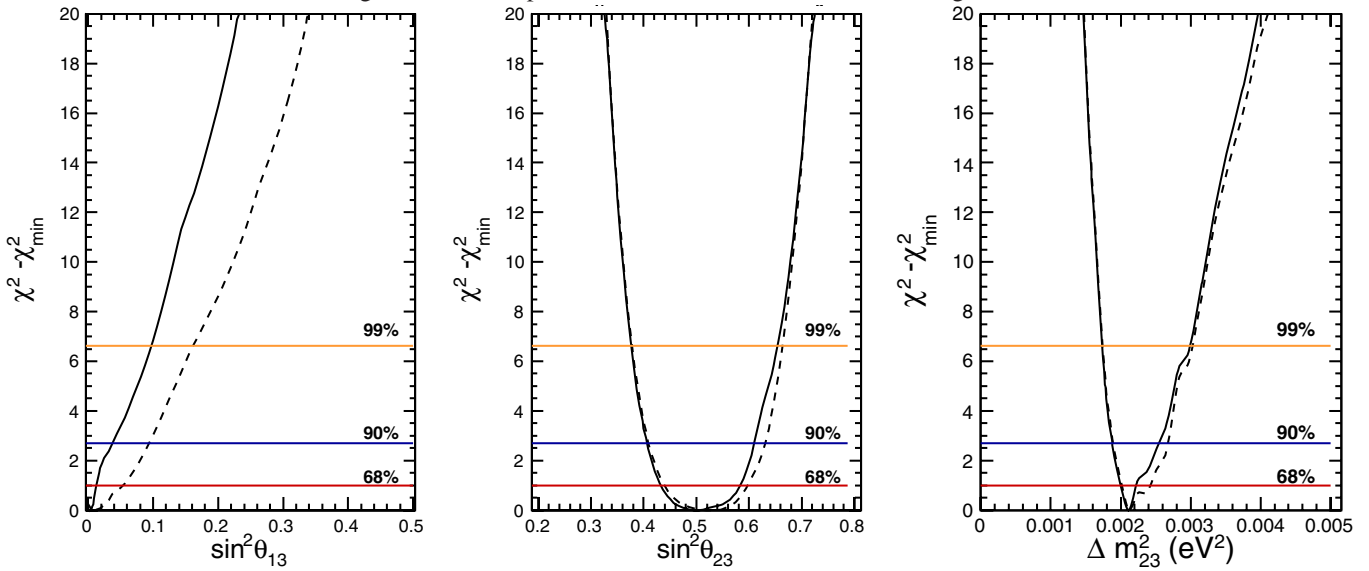


FIG. 9 (color online). The  $\Delta \chi^2$  distributions for the SK-I + II + III data set in the normal (solid) and inverted (dashed) hierarchies. The horizontal lines represent the position of the one-dimensional cut value corresponding to the (from top to bottom) 99%, 90%, and 68% CL.

best fit in the normal hierarchy is at  $\Delta m^2 = 2.1 \times 10^{-3} \text{ eV}^2$ ,  $\sin^2\theta_{13} = 0.0$ , and  $\sin^2\theta_{23} = 0.5$  with  $\chi^2_{\min} = 468.7$ . In the inverted hierarchy, the fit is at  $\Delta m^2 = 2.1 \times 10^{-3} \text{ eV}^2$ ,  $\sin^2\theta_{13} = 0.006$ , and  $\sin^2\theta_{23} = 0.53$ . The results are summarized in Table IV. No preference is seen in the data for either mass hierarchy. Confidence intervals at 90% (99%) are drawn in two dimensions at  $\chi^2 = \chi^2_{\min} + 4.6(9.2)$  and the third parameter point in these projections has been minimized over at each point in the plane to give the smallest value of  $\chi^2$ . Computing the 90% (99%) critical value using a Feldman-Cousins [47] type procedure confirmed that 4.6 (9.2) is the correct value in this scheme. The

resulting allowed regions and corresponding  $\Delta\chi^2$  distributions are shown in Figs. 7–9. In the first panel of the former two figures, the  $\Delta m^2$  vs  $\theta_{13}$  plane for the fit is overlaid with the Chooz [23] 90% C.L. exclusion contour. The zenith angle distributions of the combined data overlaid with the best-fit MC expectation in the normal hierarchy and the expectation resulting from  $\theta_{13}$  at the Chooz limit are shown in Fig. 10. Figure 11 shows the up-down asymmetry for the single-ring (multiring)  $e$ -like sample as a function of lepton momentum (total energy) for the single-ring (multiring) sample. The data are consistent with  $\sin^2\theta_{13} = 0$ .

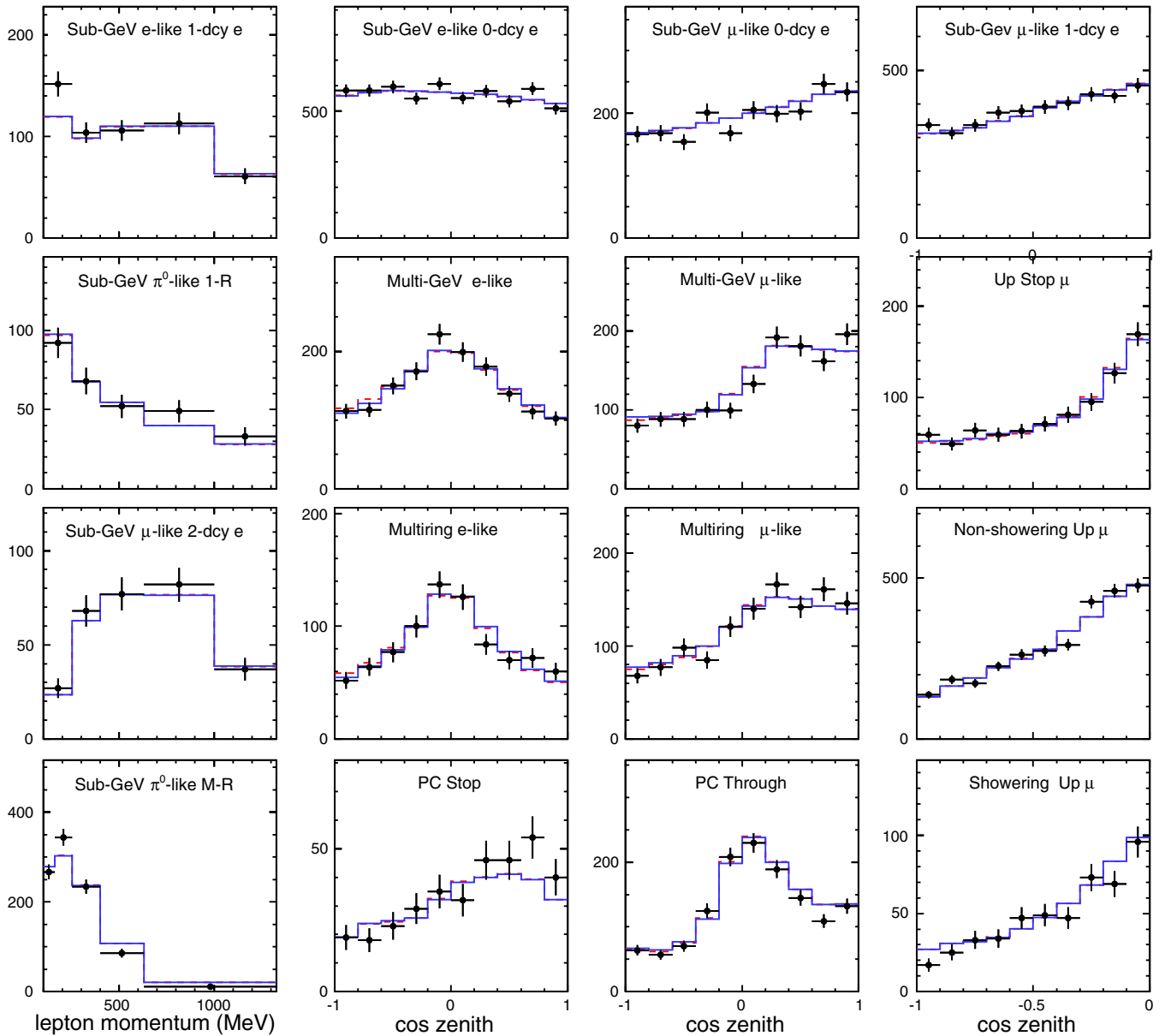


FIG. 10 (color online). SK-I + II + III zenith angle and lepton momentum distributions of the event samples used in the analyses. Black dots represent the data with statistical errors, the solid lines are the MC expectation at the best fit from the  $\theta_{13}$  analysis, and dashed lines show the expectation at the best-fit atmospheric variables but with  $\theta_{13}$  at the Chooz limit.

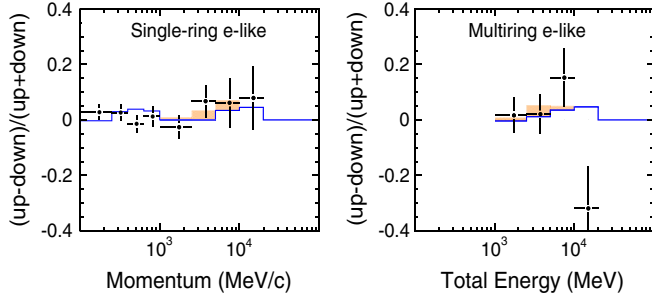


FIG. 11 (color online). Asymmetry  $(\text{up} - \text{down})/(\text{up} + \text{down})$  for the SK-I + II + III data set. Up is defined as events with  $\cos\Theta < -0.2$  and down as  $\cos\Theta > 0.2$ . Solid lines represent the MC expectation at the best fit from the  $\theta_{13}$  analysis and the shaded regions show the expectation at the best-fit atmospheric variables but with  $\theta_{13}$  at the Chooz limit for the single (multi) ring  $e$ -like events at left (right). Error bars are statistical.

## V. CONCLUSION

A three-flavor oscillation fit to the first, second, and third generation Super-K atmospheric neutrino data has been performed. No evidence for  $\theta_{13} > 0$  is found in fits to either hierarchy. The best-fit oscillation parameters in the normal (inverted) hierarchy are  $\Delta m^2 = 2.1 \times 10^{-3} \text{ eV}^2$ ,  $\sin^2\theta_{13} = 0.0(0.006)$ , and  $\sin^2\theta_{23} = 0.5(0.53)$ . The value of  $\theta_{13}$  is constrained to  $\sin^2\theta_{13} < 0.04(0.09)$  at the 90% confidence level. All fits are consistent with the Chooz experiment's upper limit and no preference for either mass hierarchy exists in the data. The  $\theta_{23}$  octant analysis finds no evidence for a preferred octant for  $\theta_{23}$ . However, the mixing angle is constrained at 90% C.L. to  $0.407 \leq \sin^2\theta_{23} \leq 0.583$ .

## ACKNOWLEDGMENTS

We gratefully acknowledge the cooperation of the Kamioka Mining and Smelting Company. The Super-Kamiokande experiment has been built and operated from funding by the Japanese Ministry of Education, Culture, Sports, Science and Technology, the United States Department of Energy, and the U.S. National Science Foundation. Some of us have been supported by funds from the Korean Research Foundation (BK21), and the Korea Science and Engineering Foundation. Some of us have been supported by the State Committee for Scientific Research in Poland (Grant No. 1757/B/H03/2008/35).

## APPENDIX

Tables V, VI, and VII summarize the best-fit systematic error parameters for the best-fit point in the normal hierarchy fit from the  $\theta_{13}$  analysis.

TABLE V. Flux-related systematic errors that are common to all SK geometries. The second column shows the best-fit value of the systematic error parameter  $\epsilon_i$  in percent and the third column shows the estimated 1- $\sigma$  error size in percent.

Systematic error		Fit value	$\sigma$		
Flux normalization	$E_\nu < 1 \text{ GeV}$	34.7	25 <sup>a</sup>		
	$E_\nu > 1 \text{ GeV}$	8.8	7 <sup>b</sup>		
$\nu_\mu/\nu_e$	$E_\nu < 1 \text{ GeV}$	-1.9	2		
	$1 < E_\nu < 10 \text{ GeV}$	-2.5	3		
	$E_\nu > 10 \text{ GeV}$	-3.7	5 <sup>c</sup>		
$\bar{\nu}_e/\nu_e$	$E_\nu < 1 \text{ GeV}$	5.54	5		
	$1 < E_\nu < 10 \text{ GeV}$	1.13	5		
	$E_\nu > 10 \text{ GeV}$	-0.10	8 <sup>d</sup>		
$\bar{\nu}_\mu/\nu_\mu$	$E_\nu < 1 \text{ GeV}$	-0.48	2		
	$1 < E_\nu < 10 \text{ GeV}$	-1.35	6		
	$E_\nu > 10 \text{ GeV}$	-1.75	6 <sup>c</sup>		
	Up/down ratio	<400 MeV	$e$ -like	-0.07	0.1
			$\mu$ -like	-0.23	0.3
		>400 MeV	0-decay $\mu$ -like	-0.84	1.1
			$e$ -like	-0.61	0.8
		Multi-GeV	$\mu$ -like	-0.38	0.5
			0-decay $\mu$ -like	-1.29	1.7
	Multiring sub-GeV	$e$ -like	-0.53	0.7	
		$\mu$ -like	-0.15	0.2	
	Multiring multi-GeV	$\mu$ -like	-0.15	0.2	
$e$ -like		-0.23	0.3		
Horizontal/vertical ratio	PC	$\mu$ -like	-0.15	0.2	
		$e$ -like	-0.01	0.1	
	<400 MeV	$\mu$ -like	-0.01	0.1	
		0-decay $\mu$ -like	-0.03	0.3	
	>400 MeV	$e$ -like	-0.14	1.4	
		$\mu$ -like	-0.19	1.9	
	Multi-GeV	0-decay $\mu$ -like	-0.14	1.4	
		$e$ -like	-0.33	3.2	
	Multiring sub-GeV	$\mu$ -like	-0.23	2.3	
		$\mu$ -like	-0.13	1.3	
	Multiring multi-GeV	$e$ -like	-0.29	2.8	
		$\mu$ -like	-0.15	1.5	
PC	$e$ -like	-0.17	1.7		
	$\mu$ -like	-12.9	10 <sup>f</sup>		
K/ $\pi$ ratio in flux calculation					
Neutrino path length		-8.8	10		
Sample-by-sample	FC multi-GeV	-4.5	5		
	PC + Up-stop $\mu$	-7.1	5		

<sup>a</sup>Uncertainty linearly decreases with  $\log E_\nu$  from 25% (0.1 GeV) to 7% (1 GeV).

<sup>b</sup>Uncertainty is 7% up to 10 GeV, linearly increases with  $\log E_\nu$  from 7% (10 GeV) to 12% (100 GeV) and then to 20% (1 TeV).

<sup>c</sup>Uncertainty linearly increases with  $\log E_\nu$  from 5% (30 GeV) to 30% (1 TeV).

<sup>d</sup>Uncertainty linearly increases with  $\log E_\nu$  from 8% (100 GeV) to 20% (1 TeV).

<sup>e</sup>Uncertainty linearly increases with  $\log E_\nu$  from 6% (50 GeV) to 40% (1 TeV).

<sup>f</sup>Uncertainty increases linearly from 5% to 20% between 100 GeV and 1 TeV.

TABLE VI. Neutrino interaction and particle production systematic errors that are common to all SK geometries. The second column shows the best-fit value of the systematic error parameter  $\epsilon_i$  in percent and the third column shows the estimated  $1\text{-}\sigma$  error size in percent.

Systematic error			Fit value	$\sigma$
MA in QE and single $\pi$			-2.4	10
CCQE cross section			0.66	1.0 <sup>a</sup>
Single meson production cross section			7.8	20
DIS cross section ( $E_{\text{nu}} < 10$ GeV)			-0.16	1.0 <sup>b</sup>
DIS cross section			2.27	5
Coherent $\pi$ production			1.53	100
NC/(CC)			1.51	20
Nuclear effect in $^{16}\text{O}$ nucleus			-13.8	30
Nuclear effect in pion spectrum			0.8	1.0 <sup>c</sup>
$\nu_\tau$ contamination			1.0	30
NC in FC $\mu$ -like (hadron simulation)			-4.6	10
CCQE $\bar{\nu}_i/\nu_i$ ( $i = e, \mu$ ) ratio			0.84	1.0 <sup>a</sup>
CCQE $\mu/e$ ratio			1.12	1.0 <sup>a</sup>
Single $\pi$ production, $\pi^0/\pi^\pm$ ratio			-29.0	40
Single $\pi$ production, $\bar{\nu}_i/\nu_i$ ( $i = e, \mu$ ) ratio			-0.04	1.0 <sup>d</sup>
$\pi^+$ decay uncertainty	Sub-GeV 1-ring	$e$ -like 0-decay	-0.48	0.5
		$\mu$ -like 1-decay	0.77	-0.8
		$e$ -like 1-decay	3.9	-4.1
		$\mu$ -like 0-decay	-0.77	0.8
		$\mu$ -like 2-decay	5.46	-5.7

<sup>a</sup>Difference from the Nieves [41] model is set to 1.0.

<sup>b</sup>Difference from Capella-Kaidalov-Merino-Tran Thanh Van [42] parametrization is set to 1.0.

<sup>c</sup>Difference between NEUT [43] and NUANCE [44] is set to 1.0.

<sup>d</sup>Difference from the Hernandez [45] model is set to 1.0.

TABLE VII. Systematic errors that are independent between SK-I, SK-II, and SK-III. Columns labeled “Fit” show the best-fit value of the systematic error parameter  $\epsilon_i$  in percent. Those labeled “ $\sigma$ ” show the estimated  $1\text{-}\sigma$  error size in percent.

Systematic error			SK-I		SK-II		SK-III	
			Fit	$\sigma$	Fit	$\sigma$	Fit	$\sigma$
FC reduction			0.005	0.2	0.008	0.2	0.061	0.8
PC reduction			-0.99	2.4	-2.12	4.8	0.034	0.5
FC/PC separation			-0.058	0.6	0.068	0.5	-0.28	0.9
PC-stop/PC-through separation (top)			7.84	14	-17.47	21	-20.03	31
PC-stop/PC-through separation (barrel)			-2.27	7.5	-31.51	17	3.44	23
PC-stop/PC-through separation (bottom)			-2.32	11.	-7.32	12	1.59	11
Non- $\nu$ background (BG) ( $e$ -like)	Sub-GeV		0.077	0.5	0.004	0.2	0.003	0.1
	Multi-GeV		0.047	0.3	0.005	0.3	0.011	0.4
Non- $\nu$ BG ( $\mu$ -like)	Sub-GeV		-0.01	0.1	0.02	0.1	0.052	0.1
	Multi-GeV		-0.01	0.1	0.02	0.1	0.11	0.2
	Sub-GeV 1-ring	$\mu$ -like 0-decay	-0.04	0.4	0.02	0.1	0.052	0.1
	PC		-0.02	0.2	0.14	0.7	0.95	1.8
Fiducial volume			-0.23	2	0.43	2	0.93	2
Ring separation	<400 MeV	$e$ -like	1.23	2.3	-1.67	1.3	0.12	2.3
		$\mu$ -like	0.37	0.7	-2.96	2.3	0.037	0.7
	>400 MeV	$e$ -like	0.21	0.4	-2.19	1.7	0.021	0.4
		$\mu$ -like	0.37	0.7	-0.90	0.7	0.036	0.7
	Multi-GeV	$e$ -like	1.97	3.7	-3.35	2.6	0.19	3.7
		$\mu$ -like	0.91	1.7	-2.19	1.7	0.089	1.7
	Multiring sub-GeV	$\mu$ -like	-2.40	-4.5	10.56	-8.2	-0.24	-4.5
	Multiring multi-GeV	$e$ -like	0.05	0.1	-2.45	1.9	0.16	3.1
$\mu$ -like		-2.19	-4.1	1.03	-0.8	-0.21	-4.1	

TABLE VII. (Continued)

Systematic error			SK-I		SK-II		SK-III	
			Fit	$\sigma$	Fit	$\sigma$	Fit	$\sigma$
Particle identification	Sub-GeV	$e$ -like	-0.007	0.1	0.13	0.5	0.004	0.1
		$\mu$ -like	0.007	-0.1	-0.13	-0.5	-0.004	-0.1
	Multi-GeV	$e$ -like	-0.014	0.2	0.023	0.1	0.008	0.2
		$\mu$ -like	0.014	-0.2	-0.023	-0.1	-0.008	-0.2
Particle identification (multiring)	Sub-GeV	$\mu$ -like	-0.18	-3.9	-0.55	-2.2	-0.15	-3.9
	Multi-GeV	$e$ -like	0.078	1.7	0.45	1.8	0.063	1.7
		$\mu$ -like	-0.13	-2.9	-0.86	-3.4	-0.11	-2.9
Energy calibration			-0.002	1.1	-0.56	1.7	-0.35	2.7
Up/down asymmetry energy calibration			-0.4	0.6	-0.15	0.6	-0.03	1.3
Upward-going muon reduction	Stopping Through-going		-0.057	0.7	-0.14	0.7	0.14	0.7
			-0.041	0.5	-0.10	0.5	0.10	0.5
Upward-stopping/through-going $\mu$ separation			-0.04	0.4	0.006	0.4	0.04	0.6
Energy cut for upward-stopping $\mu$			-0.13	0.8	-0.26	1.4	0.78	2.1
Path length cut for upward through-going $\mu$			0.39	1.8	-1.0	2.1	0.4	1.6
Upward through-going $\mu$ showering separation			9.42	9.0	2.28	13.0	6.1	6.0
BG subtraction of upward $\mu^a$	Stopping		4.16	16	-7.47	21	0.004	20
	Nonshowering		-1.24	11	8.08	15	6.34	19
	Showering		2.27	18	-18.16	14	24.7	24
Multi-GeV single-ring electron BG			5.95	16.3	-4.67	23.4	1.06	41.4
Multi-GeV multiring electron BG			-4.38	35.6	-1.4	22.3	-16.8	38.0
Multi-GeV multiring $e$ -like likelihood			-1.12	6.4	0.5	11.1	-0.3	5.3
Sub-GeV 1-ring $\pi^0$ selection	100 < $P_e$ < 250	MeV/c	-3.94	11.2	-4.08	7.5	-5.34	7.7
	250 < $P_e$ < 400		-4.05	11.5	-4.85	8.9	-18.37	26.4
	400 < $P_e$ < 630		-8.23	23.4	-9.52	17.5	-8.70	12.5
	630 < $P_e$ < 1000		-6.72	19.1	-5.81	10.7	-18.58	26.7
	1000 < $P_e$ < 1330		-4.57	13.0	-6.03	11.1	-18.58	26.7
Sub-GeV 2-ring $\pi^0$			-0.31	2	0.024	2	0.009	1
Decay-e tagging			0.16	1.5	0.41	1.5	1.06	1.5
Solar activity			0.6	20	27.9	50	3.78	20

<sup>a</sup>The uncertainties in BG subtraction for upward-going muons are only for the most horizontal bins  $-0.1 < \cos\theta < 0$ .

- [1] B. T. Cleveland *et al.* (Homestake Collaboration), *Astrophys. J.* **496**, 505 (1998).
- [2] J. N. Abdurashitov *et al.* (SAGE Collaboration), *Phys. Rev. C* **80**, 015807 (2009).
- [3] W. Hampel *et al.* (GALLEX Collaboration), *Phys. Lett. B* **447**, 127 (1999).
- [4] M. Altmann *et al.* (GNO Collaboration), *Phys. Lett. B* **616**, 174 (2005).
- [5] J. Hosaka *et al.* (Super-Kamiokande Collaboration), *Phys. Rev. D* **73**, 112001 (2006).
- [6] J. P. Cravens *et al.* (Super-Kamiokande Collaboration), *Phys. Rev. D* **78**, 032002 (2008).
- [7] B. Aharmim *et al.* (SNO Collaboration), *Phys. Rev. C* **72**, 055502 (2005).
- [8] B. Aharmim *et al.* (SNO Collaboration), arXiv:0910.2984 [Phys. Rev. C (to be published)].
- [9] S. Abe *et al.* (KamLAND Collaboration), *Phys. Rev. Lett.* **100**, 221803 (2008).
- [10] J. Hosaka *et al.* (Super-Kamiokande Collaboration), *Phys. Rev. D* **74**, 032002 (2006).
- [11] Y. Ashie *et al.* (Super-Kamiokande Collaboration), *Phys. Rev. D* **71**, 112005 (2005).
- [12] M. H. Ahn *et al.* (K2K Collaboration), *Phys. Rev. D* **74**, 072003 (2006).
- [13] P. Adamson *et al.* (MINOS Collaboration), *Phys. Rev. Lett.* **101**, 131802 (2008).
- [14] Y. Itow *et al.* (T2K Collaboration), arXiv:hep-ex/0106019.
- [15] F. Ardellier *et al.* (Double Chooz Collaboration), arXiv:hep-ex/0606025.
- [16] X. Guo *et al.* (Daya Bay Collaboration), arXiv:hep-ex/07101029.
- [17] D. S. Ayres *et al.* (NOvA Collaboration), arXiv:hep-ex/0503053.
- [18] S. B. Kim *et al.* (RENO Collaboration), *J. Phys. Conf. Ser.* **120**, 052025 (2008).
- [19] M. Komatsu, P. Migliozzi, and F. Terranova, *J. Phys. G* **29**,

- 443 (2003).
- [20] S. Yamamoto *et al.* (K2K Collaboration), *Phys. Rev. Lett.* **96**, 181801 (2006).
- [21] F. Boehm *et al.* (Palo Verde Collaboration), *Phys. Rev. D* **64**, 112001 (2001).
- [22] P. Adamson *et al.* (MINOS Collaboration), *Phys. Rev. Lett.* **103**, 261802 (2009).
- [23] M. Apollonio *et al.* (Chooz Collaboration), *Eur. Phys. J. C* **27**, 331 (2003).
- [24] V. Barger, D. Marfatia, and K. Whisnant, *Phys. Rev. D* **65**, 073023 (2002).
- [25] B. Pontecorvo, *Zh. Eksp. Teor. Fiz.* **53**, 1717 (1967) [*Sov. Phys. JETP* **26**, 984 (1968)].
- [26] Z. Maki, M. Nakagawa, and S. Sakata, *Prog. Theor. Phys.* **28**, 870 (1962).
- [27] O. L. G. Peres and A. Y. Smirnov, *Phys. Lett. B* **456**, 204 (1999).
- [28] T. Schwetz, M. Tortola, and J. W. Valle, *New J. Phys.* **10**, 113011 (2008).
- [29] C. Giunti, C. W. Kim, and M. Monteno, *Nucl. Phys.* **B521**, 3 (1998).
- [30] V. Barger, K. Whisnant, S. Pakvasa, and R. J. N. Phillips, *Phys. Rev. D* **22**, 2718 (1980).
- [31] A. M. Dziewonski and D. L. Anderson, *Phys. Earth Planet. Inter.* **25**, 297 (1981).
- [32] Y. Fukuda *et al.* (Super-Kamiokande Collaboration), *Nucl. Instrum. Methods Phys. Res., Sect. A* **501**, 418 (2003).
- [33] Y. Ashie *et al.* (Super-Kamiokande Collaboration), *Phys. Rev. Lett.* **93**, 101801 (2004).
- [34] S. Desai *et al.* (Super-Kamiokande Collaboration), *Astropart. Phys.* **29**, 42 (2008).
- [35] C. Berger and L. M. Sehgal, *Phys. Rev. D* **76**, 113004 (2007).
- [36] K. S. Kuzmin *et al.*, *Mod. Phys. Lett. A* **19**, 2815 (2004).
- [37] M. Glück, E. Reya, and I. Schienbein, *Eur. Phys. J. C* **5**, 461 (1998).
- [38] M. Honda, T. Kajita, K. Kasahara, S. Midorikawa, and T. Sanuki, *Phys. Rev. D* **75**, 043006 (2007).
- [39] T. Barszczak, Ph.D. thesis, University of California, Irvine, 2005.
- [40] G. L. Fogli, E. Lisi, A. Marrone, D. Montanino, and A. Palazzo, *Phys. Rev. D* **66**, 053010 (2002).
- [41] J. Nieves, J. E. Amaro, and M. Valverde, *Phys. Rev. C* **70**, 055503 (2004).
- [42] A. Capella, A. Kaidalov, C. Merino, and J. Tran Thanh Van, *Phys. Lett. B* **337**, 358 (1994).
- [43] Y. Hayato, *Nucl. Phys. B, Proc. Suppl.* **112**, 171 (2002).
- [44] D. Casper, *Nucl. Phys. B, Proc. Suppl.* **112**, 161 (2002).
- [45] E. Hernandez, J. Nieves, and M. Valverde, *Phys. Rev. D* **76**, 033005 (2007).
- [46] G. L. Fogli, E. Lisi, A. Marrone, A. Palazzo, and A. M. Rotunno, *Phys. Rev. Lett.* **101**, 141801 (2008).
- [47] G. Feldman and R. Cousins, *Phys. Rev. D* **57**, 3873 (1998).